Deterministic retrieval of surface waviness by means of topography with coherent X-rays

A. Souvorov,[a]* M. Yabashi,[a] K. Tamasaku,[b] T. Ishikawa,[b] Y. Mori,[c] K. Yamauchi,[c] K. Yamamura[c] and A. Saito[c]

[a]*SPring-8/JASRI, Kouto 1-1-1, Mikazuki, Hyogo 679-5148, Japan,* [b]*SPring-8/RIKEN, Kouto 1-1-1, Mikazuki, Hyogo 679-5148, Japan, and* [c]*Osaka University, Yamada-oka 2-1, Suita, Osaka 565-0871, Japan. E-mail: souvorov@spring8.or.jp*

A surface profile retrieval technique from multiple X-ray total reflection images taken at various distances with full coherent illumination is demonstrated. An experiment was performed using the 1 km-long BL29XU beamline at the SPring-8 facility, Japan. Obtained results are compared with results from the optical metrology technique (Fizeau's interferometer). Good agreement between X-ray and optical methods proves the validity of the current approach. Meanwhile, the sensitivity of the X-ray technique is several times higher than that of the standard one. This technique is well suited to the needs of characterizing grazing optics for new-generation X-ray sources.

1. Introduction

Rapid progress in the development of advanced X-ray sources has led to increasing concern about the performance and limitations of available optics. The high-quality photon beams produced by new-generation X-ray sources impose rigid requirements on the quality of the optical components that comprise current experimental set-ups.

One of the factors limiting the performance of any optics is the surface roughness. Surface topographic errors are generally viewed as the sum of two independent components, figure and finish (Church & Takacs, 1993). While both affect the performance of optics, the former, figure, is of primary interest for X-ray imaging techniques using grazing-incidence mirrors (Schelokov et al., 1996; Souvorov et al., 1997; Rommeveaux & Souvorov, 1999).

Unfortunately, the technology to manufacture and measure large and smooth optical surfaces did not progress as rapidly as the demands (Takacs, 1986; Assoufid, 2001). The standard metrology instruments used to characterize grazing-incidence optics include a long trace profiler and a figure interferometer. It is beyond the scope of this article to compare the numerous types of instruments used to measure surface roughness. The performance and limitations of these instruments can be found elsewhere (for example, see Bennett & Mattsson, 1989). In particular, their ability to measure the figure error of long (more than 0.1 m) and smooth (less than 1 µrad slope error) surfaces is poor due to a low signal-to-noise ratio. A fundamental obstacle that limits the performance of conventional techniques is the wavelength of radiation used to probe the surfaces. The shorter the wavelength, the greater the momentum transfer, and consequently the larger the phase modulation generated by a rough surface. X-ray wavelengths are on the same order of magnitude as the roughness of a state-of-the-art surface. Thus, until only recently, the usage of X-ray interferometry techniques was limited due to the lack of X-ray coherence. New synchrotron facilities (like SPring-8, APS and ESRF), however, have removed this limitation. Today it is feasible to perform various types of X-ray interferometric measurements with radiation wavelengths shorter than 1 Å.

The aim of this article is to demonstrate a novel technique for measuring surface waviness with extremely high sensitivity and decent precision, which is based on the numerical retrieval of the surface topology from multiple total reflection images taken at various distances with coherent X-ray illumination.

2. Theoretical framework

One issue in generating images of a rough surface with partially coherent X-rays can be considered to be part of the more global problem of scattering at a rough surface. One can distinguish several conditions that simplify this consideration. Firstly, imaging of a rough surface with hard X-rays (10–30 keV) is possible only at a glancing incidence angle, i.e. a few milliradians. Owing to this geometrical factor, the image contrast is only sensitive to the longitudinal roughness, and is composed of well pronounced one-dimensional fringes perpendicular to the incidence plane. Thus, the problem can be reduced from a two-dimensional issue to a one-dimensional one.

Secondly, because the optical transfer function in free space can be considered as a spatial frequency low-pass filter (Goodman, 1996), X-ray images are primarily formed from the contributions of roughness spatial frequencies localized in the low- and medium-frequency range (coherent specular reflection). In general, this indicates that the surface image is sensitive to roughness spatial wavelengths in the region spanning from a few centimetres down to a fraction of a millimetre. Together with the paraxial approximation of wave propagation in free space (Goodman, 1996), this facilitates numerical treatment of the problem.

An additional simplification can be achieved if the incident wave is considered as a plane monochromatic wave with linear polarization. In the case of hard X-rays, this approximation is supported by the high natural angular collimation (about 10–20 µrad) and linear polarization of synchrotron radiation generated at modern facilities, as well as by the longer distances from the source to the experimental set-up (more than 50 m).

The necessity of large distances is also dictated by requirements imposed on the high spatial resolution of the set-up. Longer distances lead to a greater coherence, and improved spatial resolutions for imaging set-ups (Pogany et al., 1997).

It has been shown that the chromaticity of incident radiation induces a smaller effect on the resolution than does the spatial coherence (Pogany et al., 1997). Thus, the incident wave from a standard double-crystal monochromator is sufficient to be regarded as quasi-monochromatic.

The more or less general scattering problem cannot be exactly solved. Therefore only approximate analytic approaches to this problem exist. Two techniques have been most widely used: perturbation theory and the quasi-classical approximation, also known as the Kirchhoff approximation (Holliday, 1987; Sánchez-Gil & Nieto-Vesperinas, 1991; Sánchez-Gil et al., 1995). In this work, the Kirchhoff-tangent plane approximation will be used in describing the problem (Voronovich, 1999). It is built on the assumption that wave reflection at each point of the surface acts as if the surface coincides with the tangent plane at each point. The value of the field and its normal derivative at the surface are then easily expressed through the incident field. The scattered field is determined using the Helmholtz formula.

Let us consider the diffraction geometry shown in Fig. 1. An incident σ-polarized plane wave with a wavevector situated in the

XZ-plane is scattered at a one-dimensional wavy surface $h(x)$ with the mean plane lying in the *XY*-plane,

$$E_{in} = \exp(ik_0x - iq_0z). \tag{1}$$

The scattering amplitude is then given by (Voronovich, 1999, ch. 5.1)

$$S(k, k_0) = \int dx\, \Re(x)\big[q + q_0 + (k - k_0)h'_x\big] \\ \times \exp\big[-i(k - k_0)x - i(q + q_0)h(x)\big], \tag{2}$$

and the reflected wave is expressed as

$$E_{sc} = (4\pi)^{-1} \int (dk/q)\, S(k, k_0) \exp(ikx + iqz), \tag{3}$$

where $k_0 = K\cos\theta_0$, $q_0 = (K^2 - k_0^2)^{1/2}$ are the components of the incident wavevector, k, $q = (K^2 - k^2)^{1/2}$ are the components of the reflected wavevector, $K = 2\pi/\lambda$, θ_0 is the glancing angle, λ is the incident wavelength and $\Re(x)$ is a local reflection coefficient,

$$\Re(x) = \frac{\sin\theta_x - (\sin^2\theta_x - 2\delta)^{1/2}}{\sin\theta_x + (\sin^2\theta_x - 2\delta)^{1/2}}, \tag{4}$$

where $\theta_x = \theta_0 + \arctan h'_x$, $h'_x = dh(x)/dx$ and δ is the refractive index decrement. Here, absorption is not taken into account.

Let the reflected wave be recorded at a distance L from the centre of the surface, in a plane perpendicular to the direction of beam propagation (see Fig. 2). Equation (3) can then be rewritten as

$$E_{sc} = (4\pi)^{-1} \exp(ik_0x + iq_0z) \\ \times \int d\eta\, [S(\eta)/q] \exp\left[i\rho\frac{\eta}{\sin\theta_0} - i\frac{L\sin\theta_0 - \rho\cos\theta_0}{2K\sin\theta_0}\left(\frac{\eta}{\sin\theta_0}\right)^2\right], \tag{5}$$

where $\eta = k - k_0$ and ρ is a coordinate in the image plane that is directed downwards.

It can be seen from (5) that the second term in the exponent introduces an asymmetry into the wave field distribution. This becomes more pronounced when the distance L is comparable with the surface length. This term arises in the scattering geometry where, owing to a small grazing incidence, the surface is positioned almost parallel to the incident and specular reflected beams, while intensity is measured in the plane normal to the reflected beam. Thus, the distance from points on the surface to the observation plane may vary significantly. This term can be labelled as a geometrical factor.

The scattering surface can also be classified as compact (enclosing some finite volume) or incompact (infinite in space). The most common theoretical approach is to consider an incompact surface that is on average planar and illuminated with a plane wave, or a compact surface illuminated with a Gaussian beam. This allows the elimination of surface-edge scattering effects. In grazing-incidence experiments, however, neither of these cases is valid, and the edge effects must be taken into account. Strictly speaking, the Kirchhoff approximation cannot be considered accurate in the vicinity of surface edges. It generally, however, provides reasonable estimates.

The goal of this work lies not only in the direct modelling of rough surface images but, additionally, in modelling inverse scattering, *i.e.* the deterministic retrieval of a surface's topology from its images. The retrieved surfaces, in turn, are intended to serve as feedback to the polishing technology. At this stage of the work, we are interested in developing techniques to characterize smooth planar surfaces that are suitable as high-quality X-ray optical elements for modern X-ray sources.

At grazing incidence, a substrate with a slightly rough surface will exhibit similar behaviour to that of a random phase screen. In small-amplitude perturbation theory, the surface is considered to be sufficiently smooth when the following conditions are fulfilled,

$$K|h(x)|\sin\theta_0 \ll 1, \tag{6}$$

$$|h'(x)| \ll 1. \tag{7}$$

For hard X-rays, condition (6) is valid for $|h| \ll 60$ Å. Taking into account the high specification parameters of planar X-ray mirrors (finish error $\sigma_h \simeq 1\text{--}2$ Å, figure error $\sigma_{h'} \simeq 1\text{--}2$ µrad), both conditions are more than satisfied.

Under these conditions, the problem can be analytically solved (Rommeveaux & Souvorov, 1999). The obtained solution is similar to the solution of the 'transport of intensity' equation (Gureyev, 1999), provided the object is perfectly transparent. Differences arise from the geometry; contrary to normal incidence, at grazing incidence the object is arranged almost parallel to the incident beam while an image is taken perpendicular to it. This introduces strong asymmetry between sections of the image situated on opposite sides of the optical axis, which is very well pronounced at short object-to-image distances. The primary limitation of the obtained solution is that it relies on a single image, taken at a short distance. In the case of an image corrupted with noise (for example, phase-amplitude noise in the incident beam), the retrieved profile will be distorted. Additionally, inherent limitations confine the applicability of this model. Therefore, a more general approach must be achieved, which is realised by employing a numerical model.

The use of iterative methods is one of the most common approaches to the phase problem. Most of these methods are based on ideas from the Gerchberg–Saxton algorithm (Gerchberg & Saxton, 1972; Fienup, 1982). Applied to a purely phase object, it can be said that
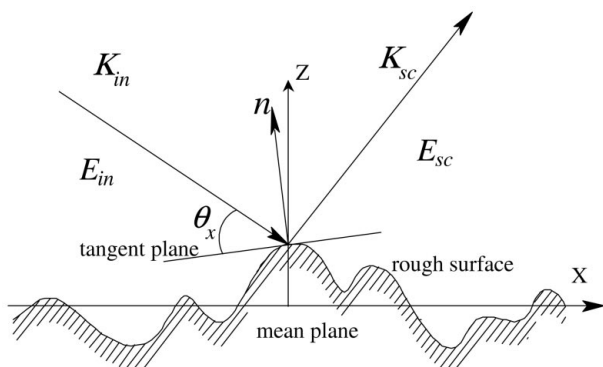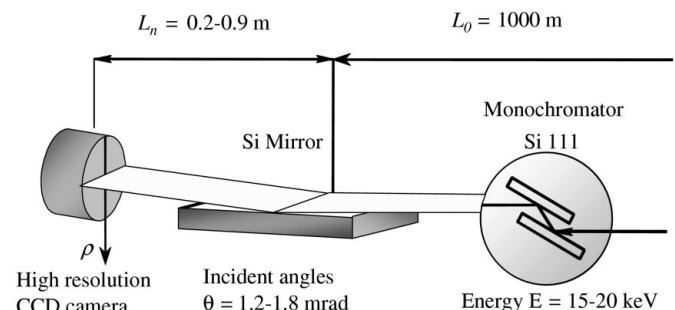

Figure 1
Scattering geometry.

Figure 2
Sketch of the experimental set-up.

this algorithm also performs phase retrieval based on a single intensity measurement. Any additional intensity measurements are redundant for the conventional Gerchberg–Saxton algorithm. As a rule, however, additional information is important in solving the inverse problem. Moreover, with respect to the grazing-incidence set-up, the geometrical factor, mentioned earlier in connection with equation (5), prevents the use of fast Fourier transforms in computations.

In the case of normal incidence, a technique of iterative phase retrieval from a set of images taken at various distances was successfully implemented using visible-light optics (Ivanov *et al.*, 1992), electron microscopy (Coene *et al.*, 1992) and X-ray holography (Cloetens *et al.*, 1999). Suppose there are several intensity distributions I_n^0 recorded at distances L_n, $n = 1, \ldots, N$. A functional J can be introduced,

$$J = \sum_{n=1}^{N} \left[\int (I_n - I_n^0)^2 \, \mathrm{d}\rho \right], \tag{8}$$

where I_n is a simulated intensity. The inverse problem can then be formulated as the retrieval of surface parameters, which minimize the functional J. The intensity profiles of 256 points were extracted from the experimental images. Here, the discrete wavelet transform coefficients of the surface function were used as the optimization parameters. Compactly supported biorthogonal spline wavelets were used for decomposition and synthesis of the surface profile. The optimal wavelet type was selected by trial and error in searching for better convergence of the iterative algorithm. The total number of fitting coefficients, however, was reduced to 144 in accordance with an effective spatial frequency bandwidth that will be discussed further. The *MATLAB* software package (The MathWorks Inc.), complete with the *Wavelet* and *Optimization* toolboxes, was used to perform numerical simulations. The advantages of using wavelet decomposition over others, such as Fourier transforms or polynomial expansion, are in the use of real coefficients, the fast numerical transform procedures and the numerical stability of the method.

3. Experiment and results

Experiments were performed at the 1 km-long beamline, BL29XUL, at the SPring-8 facility (Ishikawa *et al.*, 2001). The beamline was designed to facilitate the application of various imaging and diffraction techniques that exploit coherent properties of the X-ray beam. It is equipped with the SPring-8 standard in-vacuum undulator, which provides a photon flux of greater than 5×10^{10} photons mm^{-2} (15 keV) at the end station. The scattering geometry was situated in the vertical plane. The beamline source parameters in the vertical plane are as follows: electron beam dimension $\sigma_V = 10.1$ µm, divergence $\sigma_{V'} = 1.75$ µrad.

There are two basic parameters that limit spatial resolution in the current set-up, namely the coherence of incident radiation and the detector resolution. The incident undulator radiation can be described as a Gaussian beam to a good approximation. Its coherence is dependent on the phase-space distribution of electrons in a storage ring (Kim, 1986). When the electron beam parameters fall far from the diffraction limits, the coherence can be described using common sense by a Gaussian function. However, as the parameters approach the diffraction limits, which is the case for the new-generation sources, discrepancy from the Gaussian function can be observed (Coïsson, 1995; Takayama *et al.*, 1998). The undulator diffraction limits or, in other words, the single photon beam parameters are a spatial dimension $\sigma_R = (\lambda L)^{1/2}/4\pi$ and an angular divergence $\sigma_{R'} = (\lambda/L_U)^{1/2}$, where λ is the wavelength and L_U is the length of the

undulator. When applied to BL29XUL, this gives $\sigma_R = 1.5$ µm and $\sigma_{R'} = 4.3$ µrad at $E = 15$ keV ($\lambda = 0.83$ Å) and $L_U = 4.5$ m. It can be seen that spatial dimensions of the irradiating area σ_V remain much greater than its limit σ_R, and $\sigma_{V'}$ is significantly smaller than $\sigma_{R'}$. This indicates that at BL29XUL a well collimated relatively large electron source is available. In this case, the coherence width is only defined by the electron beam spatial size. Thus, the spatial resolution of the set-up is defined by the 'geometric unsharpness' effect or the penumbra, and can be evaluated as $\sigma_L = (L_1/L_0)\sigma_S$ where L_0 is the source-to-object distance, L_1 is the object-to-image distance and $\sigma_S = (\sigma_V^2 + \sigma_R^2)^{1/2}$. For example, taking $L_0 = 1000$ m, $L_1 = 1$ m and $\sigma_S \simeq 10$ µm, one obtains $\sigma_L \simeq 0.01$ µm.

To acquire images of the sample substrates, an X-ray zooming tube (C5333, Hamamatsu Co.) was used (Matsumura *et al.*, 1998). The zooming tube is a two-dimensional X-ray detector operational in the energy range 4–20 keV, with a highest spatial resolution less than $\sigma_D < 0.5$ µm. The magnification factor is tunable and can be easily changed from 10 to 200. The observable area is about 2.5 mm in diameter and can be easily searched at different magnifications for a region of interest by means of deflecting coils. The tube functions in the following manner: an X-ray image projected on the CsI photo-cathode is converted into a photoelectron image. In turn, the photoelectron image is magnified using the zooming coil assembly and focused on a microchannel plate (MCP). The magnified image is then intensified by the MCP, and transferred onto the phosphor screen that is monitored by a CCD camera. Owing to the massive magnetic coils, the zooming tube has large dimensions (~ 1 m length and 0.4 m by 0.4 m width by height) and a heavy weight (~ 140 kg). This makes it inconvenient to handle around the experimental set-up. Thus, a special support table was designed which provides fine two-dimensional alignment around an optical axis and precise positioning along the axis. Its design enables angular correction of the tube axis in all three planes within a range of several degrees.

Two substrates were examined. The substrates were fabricated at the Ultra Precision Machining Centre of Osaka University, Japan. The objective of this research centre is to establish new ultraprecision machining and thin-film technologies that can be used to produce perfect surfaces. The two processes mainly involved in substrate preparation are plasma chemical vaporization machining (CVM) (Mori *et al.*, 1993; Mori, Yamamura & Sano, 2000; Mori, Yamauchi *et al.*, 2000) and elastic emission machining (EEM) (Tuwa & Aketa, 1974; Mori *et al.*, 1987, 1988, 2001). EEM exhibits an excellent figuring performance, where atomic-level flatness is easily obtained without any crystallographic damage. Plasma CVM has been proposed as a precise and effective preprocess for EEM finishing. The substrates were cut out of Si bulk in the form of rectangular disks of length 100 mm, width 50 mm and height 10 mm. The surface was oriented along the (001) crystallographic planes. Working lengths of the machined surfaces varied around 90 mm.

A sketch of the experimental set-up is shown in Fig. 2. The first substrate was set at glancing angle $\theta = 1.74$ mrad with incident energy $E = 15$ keV. The second was set at $\theta = 1.2$ mrad with $E = 20$ keV. As discussed above, the ultimate spatial resolution of the set-up is defined uniquely by the detector resolution. Taking into account the small sample aperture at grazing incidence (maximum 1 mm), and the longer distance to the beamline end station ($L_0 = 1000$ m), the incident wave can be well represented as a plane monochromatic wave (divergence < 1 µrad) with linear polarization. Energies and angles were chosen using the following considerations. The optical transfer function can be considered as a linear filter acting on transmitted frequencies (Goodman, 1996). In the case of grazing incidence, the maximum contribution to the image contrast comes from the

roughness spatial wavelength around $\tau = (2\lambda L)^{1/2}/\sin\theta_0$. Contrary to the normal-incidence geometry, there is an additional parameter, the glancing angle, which can be used to change scattering conditions. To achieve maximum momentum transfer or maximum phase contrast in the scattered wave $Q = 2K\sigma_h \sin\theta_0$ (σ_h is the roughness RMS), the glancing angle must be kept close to the critical angle. In turn, the critical angle $\sin\theta_c = (2\delta)^{1/2}$ is almost linearly proportional to the incident radiation wavelength λ ($\delta \simeq \lambda^2$). Thus, the effective spatial wavelength at the critical angle is $\tau = C(2L/\lambda)^{1/2}$, where C is a constant. Thus, the sensitivity of the set-up, with respect to the high spatial frequencies of roughness, may be improved while maintaining the phase contrast at a maximum by reducing the distance to the surface L and increasing the incident radiation wavelength λ. Similarly, to see better low spatial frequencies, the distance L must be increased and the wavelength decreased.

For each substrate, a set of images ($N = 17$) was obtained separated by $\Delta L = 50$ mm, starting from a minimal gap $L_1 = 170$ mm between the surface centre and the photocathode of the zooming tube. In accordance with the above speculations, the upper limit of the roughness spatial frequencies that effectively contribute in image formation can be defined as $\tau_{min} = (\lambda L_1)^{1/2}/\sin\theta_0$ (Souvorov *et al.*, 1997). This gives $\tau_{min} = 2.2$ mm and $\tau_{min} = 2.7$ mm for the first and second substrates, respectively. Images were taken with a magnification factor $M = 60$ to ensure pixel sizes of 0.2 µm. The total spatial resolution of the detector was $\sigma_d = 0.6$ µm. As an example, one of the original images is shown in Fig. 3.

After extracting intensity profiles from the images, the inverse scattering algorithm was applied. A perfectly flat long surface was taken as the starting point. An iterative procedure was continued until no further improvement was observed. The length of the reflecting area automatically shrinks to correspond with the recorded images. The ultimate difference between simulated and measured intensities, averaged over all images, varied within $\sigma_{\Delta I} \simeq 3$–5% depending on the measurement set. An example of the original intensity distribution and a simulation is shown in Fig. 4(*a*). The simulated intensity curve is shifted downwards by 0.2 to enhance clarity of the comparison. The experimental intensities varied up to $\sigma_I \simeq 19\%$. The differential intensity $I_{dif} = I_{exp} - I_{sim}$ between experimental and simulated data is shown in Fig. 4(*b*). The standard deviation of the intensity discrepancy is $\sigma_{\Delta I} = 3.5\%$ over the total reflection area. This discrepancy can be attributed to noise in the original images. Unfortunately, the presence of coherent noise results in poor divergence of the algorithm. It took several hours and thousands of iterations to obtain the final results. The algorithm works three to five times faster with numerically simulated images. The coherent noise is generated by all optical elements installed
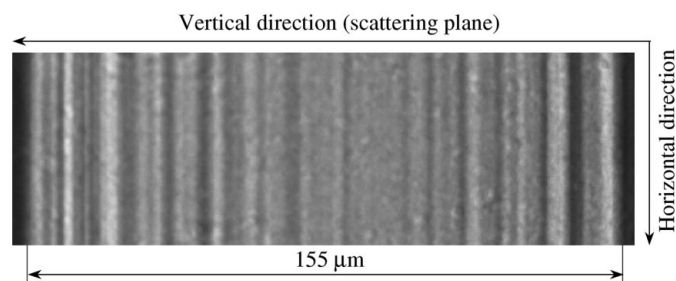
upstream from the sample position. The main source of noise, however, lies in the vacuum windows. In the case of normal incidence, influence from the vacuum windows can be reduced by taking images immediately after an object or in the object plane. In the case of grazing incidence, this is difficult as the object is elongated along the optical axis. In addition, the mirror flips up and down in a reflected beam.

For the first substrate, its central section was investigated by means of the Fizeau's interferometer prior to the experiment. The interferometer was calibrated within ± 1 nm accuracy over a 150 mm longitudinal range. Some environmental instabilities, however, generated ± 0.5 nm fluctuations in the measurements. Therefore, the accuracy of the expected slope measurement was limited to 1 µrad. A comparison of surface profiles (actually, residuals after removing the second-order fitting curve) obtained with the optical interferometer and by X-ray topography is shown in Fig. 5. Good agreement between the two profiles is observed. The surface-height standard deviation measured with the interferometer is $\sigma_h^{(i)} \simeq 5.3$ Å, while when measured with X-rays is $\sigma_h^{(x)} \simeq 5.5$ Å. The difference in surface heights between the two measurements has a standard deviation of $\sigma_{\Delta h} \simeq 3$ Å. Figure error of the optically measured profile is $\sigma_{sl} \simeq 1.1$ µrad. This agrees well with the expected slope-measurement accuracy. The X-ray measurements, however, give $\sigma_{sl} \simeq 0.8$ µrad, already an improvement to the resolution of the optical method. While the optical measurements were performed at the limit of resolution, the X-ray technique maintains potential for improvement.

For the second substrate, images were taken at two sample positions: normal and inverted, *i.e.* when the sample was inverted by 180°

Figure 4
(*a*) An intensity profile (solid line) of an image taken at a distance $L = 0.68$ m from the mirror compared with simulation (dashed line). The simulated plot is shifted downwards by 0.2 to make the comparison more clear. Intensity variation generates $\sigma_I \simeq 19\%$. (*b*) Differential intensity $I_{dif} = I_{exp} - I_{sim}$ between experimental and simulated data. The intensity discrepancy is $\sigma_{\Delta I} = 3.5\%$ over the total reflection area.
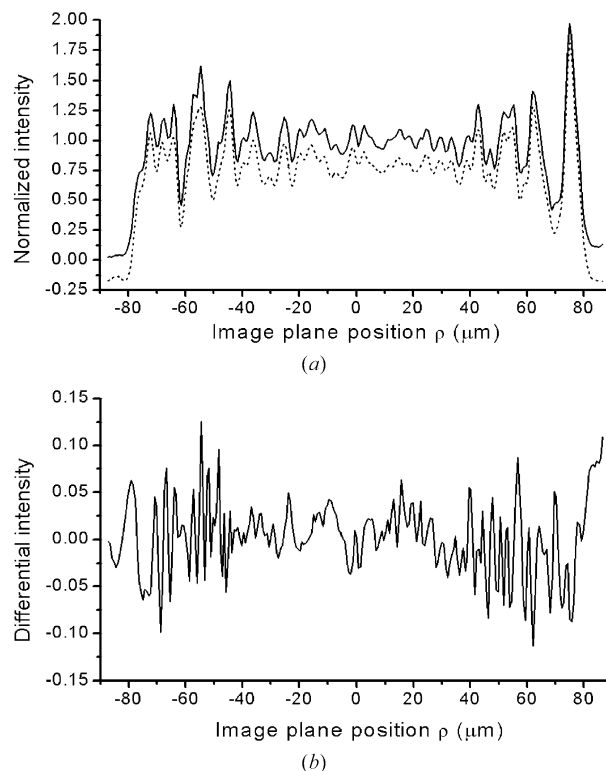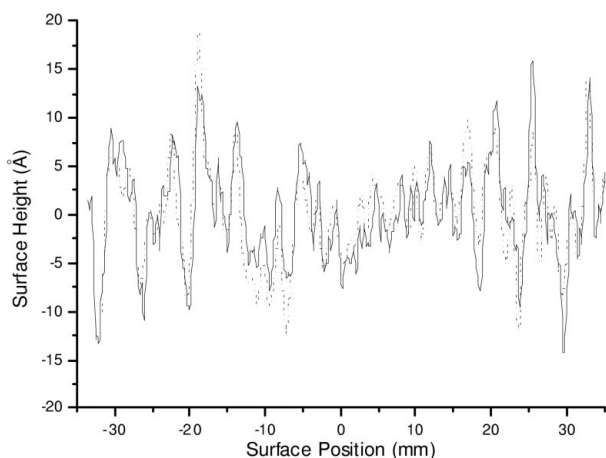

Figure 3
Example of an X-ray image taken at a distance $L = 0.43$ m from the substrate centre. An incident X-ray beam is reflected up in the vertical direction. Surface waviness generates one-dimensional fringes perpendicular to the incidence plane.
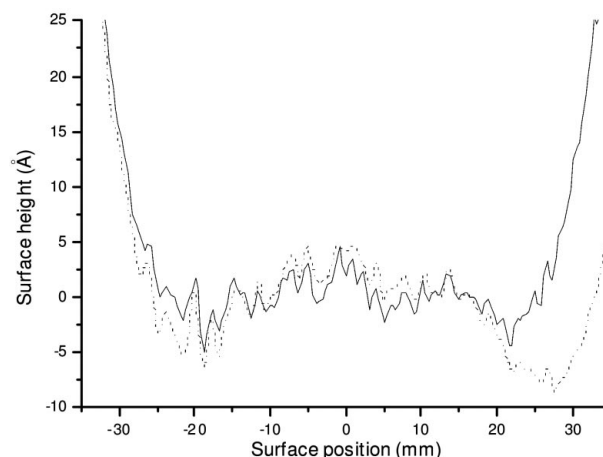
Figure 5
Comparison of surface profiles obtained by an optical interferometer (solid line) and X-ray topography (dashed line). The difference in surface heights between the two measurements has a standard deviation of $\sigma_{\Delta h} \simeq 3$ Å.

around the axis perpendicular to the surface. The substrate was oriented so that both measurements covered an almost identical sample area (± 0.1 mm lateral error in positioning). The retrieved surface profiles are shown in Fig. 6. Within the central ± 20 mm area, height standard deviations at the normal and inverted position are $\sigma_h^{(1)} \simeq 1.7$ Å and $\sigma_h^{(2)} \simeq 2.4$ Å, respectively. The difference in surface heights between two measurements has a standard deviation of $\sigma_{\Delta h} \simeq 1.3$ Å. Apart from a discrepancy at one of the edges, the obtained profiles correlate well with each other.

4. Conclusions

The presented results provide straightforward evidence of the very high sensitivity of X-rays to waviness in the surfaces of grazing-incidence optics. Sensitivity with the conventional metrology technique can be compared on the basis of the signal-to-noise ratio. For X-ray measurements, the ratio between intensity variation $\sigma_I \simeq 19\%$ and noise (discrepancy) $\sigma_{\Delta I} \simeq 3\%$ comprises a factor of six. For optical metrology, what is measured directly is a slope error. Thus, the ratio of the measured figure error $\sigma_{sl} \simeq 1.1$ µrad with the measurement accuracy $\sigma \simeq 1$ µrad provides a figure of merit of the method. By this means, it can be said that the X-ray metrology technique is at least six times more sensitive to the smooth waviness of surfaces than optical metrology. This factor can be further increased if coherent noise in the X-ray incident beam is decreased. A similar ratio can be obtained starting from a different approach. The phase shift between two surface areas at different heights h_1 and h_2 can be evaluated as $\Delta \varphi = 2K \Delta h \sin \theta$, where θ is an incident angle, $\Delta h = h_2 - h_1$ and $K = 2\pi/\lambda$. With visible light, the maximum phase difference is achieved at normal incidence $\Delta \varphi_o = 2K_o \Delta h$. With X-rays, however, the maximum is achieved at a critical angle $\Delta \varphi_x = 2K_x \Delta h \sin \theta_c$. Assuming a laser wavelength of $\lambda_o = 632$ nm, an X-ray wavelength of 0.1 nm and a critical angle of about 2 mrad, the ratio between the phases in X-ray and optical measurements will be $\Delta \varphi_x/\Delta \varphi_o = (\lambda_o/\lambda_x) \sin \theta \simeq 12$. This obtained ratio is two times higher than that inferred from the current experimental measurements, thus leaving significant room for improvement of the technique.

Taking into account the high demand for new technologies for fabricating and characterizing high-performance grazing-incidence X-ray optics, the advanced technique is well suited to modern requirements. First, it is based on measurements performed with

Figure 6
Comparison of surface profiles obtained from two sets of images taken at normal and inverted (the sample was inverted by $180°$ around the axis perpendicular to the surface) sample positions. The difference in surface heights between the two measurements has a standard deviation of $\sigma_{\Delta h} \simeq 1.3$ Å.

'high quality' X-rays, *i.e.* coherent X-rays. This is the radiation that modern X-ray optics must be designed for. Secondly, it provides a straightforward measure of the quality of an optical surface, *i.e.* if the reflected beam is uniform within some statistical fluctuations then the quality of the surface is superior to what is required. The good agreement found with optical metrology supports the appropriateness of this method. The authors believe that this technique will enable measurement of not only planar but profiled surfaces as well.

References

Assoufid, L. (2001). *Proc. SPIE*, **4143**, 98–102.
Bennett, J. M. & Mattsson, L. (1989). *Introduction to Surface Roughness and Scattering.* Washington, DC: Optical Society of America.
Church, E. L. & Takacs, P. Z. (1993). *Appl. Opt.* **32**, 3344–3353.
Cloetens, P., Ludwig, W., Baruchel, J., Van Dyck, D., Van Landuyt, J., Guigay, J. P. & Schlenker, M. (1999). *Appl. Phys. Lett.* **75**, 2912–2914.
Coene, W., Janssen, G., Op de Beeck, M. & Van Dyck, D. (1992). *Phys. Rev. Lett.* **69**, 3743–3746.
Coïsson, R. (1995). *Appl. Opt.* **34**, 904–908.
Fienup, J. R. (1982). *Appl. Opt.* **21**, 2758–2769.
Gerchberg, R. W. & Saxton, W. O. (1972). *Optik (Stuttgart)*, **35**, 237–246.
Goodman, J. W. (1996). *Introduction to Fourier Optics*, 2nd ed. New York: McGraw-Hill.
Gureyev, T. E. (1999). *Optik*, **110**, 263–266.
Holliday, D. (1987). *IEEE Trans. Antennas Propagat.* AP-**35**, 120–122.
Ishikawa, T., Tamasaku, K., Yabashi, M., Goto, S., Tanaka, Y., Yamazaki, H., Takeshita, K., Kimura, H., Ohashi, H., Matsushita, T. & Ohata, T. (2001). *Proc. SPIE*, **4145**, 1–10.
Ivanov, V. Yu., Sivokon, V. P. & Vorontsov, M. A. (1992). *J. Opt. Soc. Am.* A**9**, 1515–1524.
Kim, K.-J. (1986). *Nucl. Instrum. Methods Phys. Res. A*, **246**, 71–76.
Matsumura, T., Kinoshita, K., Tamura, S., Kamijo, N., Ozaki, Y. & Kihara, H. (1998). *X-ray Microscopy and Spectromicroscopy*, edited by J. Thieme, G. Schmahl, D. Rudolph & E. Umbach, pp. II-195–II-199. Berlin: Springer-Verlag.
Mori, Y., Yamamura, K. & Sano, Y. (2000). *Rev. Sci. Instrum.* **71**, 4627–4632.
Mori, Y., Yamamura, K., Yamauchi, K., Yoshii, K., Kataoka, T., Endo, K., Inagaki, K. & Kakiuchi, H. (1993). *Nanotechnology*, **4**, 225–229.
Mori, Y., Yamauchi, K. & Endo, K. (1987). *Precis. Eng.* **9**, 123–128.
Mori, Y., Yamauchi, K. & Endo, K. (1988). *Precis. Eng.* **10**, 24–28.

Mori, Y., Yamauchi, K., Yamamura, K., Mimura, H., Saito, A., Kishimoto, H., Sekito, Y., Kanaoka, M., Souvorov, A., Yabashi, M., Tamasaku, K. & Ishikawa, T. (2001). *Proc. SPIE*, **4501**. In preparation.

Mori, Y., Yamauchi, K., Yamamura, K. & Sano, Y. (2000). *Rev. Sci. Instrum.* **71**, 4620–4626.

Pogany, A., Gao, D. & Wilkins, S. W. (1997). *Rev. Sci. Instrum.* **68**, 2774–2782.

Rommeveaux, A. & Souvorov, A. (1999). *Proc. SPIE*, **3773**, 70–77.

Sánchez-Gil, J. A., Maradudin, A. A. & Méndez, E. R. (1995). *J. Opt. Soc. Am.* A**12**, 1547–1558.

Sánchez-Gil, J. A. & Nieto-Vesperinas, M. (1991). *J. Opt. Soc. Am.* A**8**, 1270–1286.

Schelokov, I., Hignette, O., Raven, C., Snigirev, A., Snigireva, I. & Souvorov, A. (1996). *Proc. SPIE*, **2805**, 282–291.

Souvorov, A., Snigireva, I. & Snigirev, A. (1997). *Proc. SPIE*, **3113**, 476–483.

Takacs, P. Z. (1986). *Nucl. Instrum. Methods Phys. Res. A*, **246**, 227–241.

Takayama, Y., Hatano, T., Miyahara, T. & Okamoto, W. (1998). *J. Synchrotron Rad.* **5**, 1187–1194.

Tuwa, H. & Aketa, Y. (1974). *Proceedings of International Conference on Production Engineering*, Tokyo, Japan. Tokyo: Japan Society for Precision Engineering.

Voronovich, A. G. (1999). *Wave Scattering from Rough Surface*, 2nd ed. New York: Springer-Verlag.